Article:
Kim, B., Walkley, B., Iuga, D. et al. (2026) New insights on the immobilization of radioactive acidic liquid waste and cesium in amorphous aluminophosphate waste form. Cement and Concrete Research, 203. 108169. ISSN: 0008-8846

https://doi.org/10.1016/j.cemconres.2026.108169

New Insights on the Immobilization of Radioactive Acidic Liquid Waste and Cesium in Amorphous Aluminophosphate Waste Form

Byoungkwan Kim[a,b*], Brant Walkley[a], Dinu Iuga[c], Raudhatul Islam Chaerun[d], Xiaobo Niu[e], and Wooyong Um[b,*]

[a]School of Chemical, Materials and Biological Engineering, The University of Sheffield, S1 3JD, United Kingdom

[b]Division of Advanced Nuclear Engineering (DANE), Pohang University of Science and Technology (POSTECH), 37673, Pohang, Republic of Korea

[c]Department of Physics, University of Warwick, Coventry, CV4 7AL, United Kingdom

[d]Nuclear Fuel Cycle Engineering Laboratories, Japan Atomic Energy Agency, Muramatsu 4-33, Tokai-mura, Naka-gun, Ibaraki, 319-1194, Japan

[e]Division of Sustainable Resources, Graduate School of Engineering, Hokkaido University, North 13, West 8, Sapporo, Hokkaido 060-8628, Japan

Co-corresponding authors:

Byoungkwan Kim - School of Chemical, Materials and Biological Engineering, The University of Sheffield, S1 3JD, United Kingdom; Email: b.kim@sheffield.ac.uk (B. Kim),

Wooyong Um - Division of Advanced Nuclear Engineering (DANE), Pohang University of Science and Technology (POSTECH), 37673, Pohang, Republic of Korea; Email: wooyongum@postech.ac.kr (W. Um)

Abstract

Radioactive acidic liquid waste (RALW), generated during the Chemical Oxidation Reduction Decontamination (CORD) and High Permanganate CORD Ultraviolet (HP-CORD UV) process of primary systems in nuclear power plants, contains various heavy metals and various radionuclides. These are typically removed by organic ion exchange resins, producing large amounts of secondary spent ion exchange resins (spent IERs) waste. This study aimed to reduce spent IER generation by directly using unpurified RALW as mixing solution for amorphous aluminophosphate (AAP) waste forms which use acidic solution as a raw material. In addition, Cs that may be present in RALW was added at 10 wt% to investigate its effect on the AAP structure. Neither the use of RALW as mixing solution nor the addition of Cs significantly altered the mechanical strength of AAP waste forms. The presence of heavy metal in RALW did not substantially change the local structure of Al and P in the AAP matrix. Multiscale characterization showed that Cs was mainly immobilized by forming amorphous cesium aluminophosphate and through physical incorporation within the AAP matrix. This research demonstrates that RALW can be effectively used in AAP waste forms and provides direct evidence of Cs immobilization mechanisms in AAP systems.

Keywords: Radioactive acidic liquid waste, waste form, Cs, immobilization, aluminophosphate

1. Introduction

The operation of a pressurized water reactor leads to the deposition of corrosion products incorporating activated species such as Co-58, Co-60, Mn-54, Fe-55, Ni-63, and Cr-51 throughout the primary coolant system [1]. These deposits called as Chalk River Unidentified Deposits (CRUD) can reduce heat transfer efficiency and contribute to the development of radiation fields, necessitating periodic decontamination. Chemical decontamination involves the use of a specifically formulated acidic solution to dissolve and remove the deposited corrosion products from the system. A range of chemical decontamination approaches have been established, employing organic acids including oxalic acid, citric acid, nitrilotriacetic acid, and ethylenediaminetetraacetic acid (EDTA) [2]. However, the use of these organic acids presents difficulties in managing the radioactive effluent produced during decontamination. For instance, EDTA reacts with radionuclides to generate metal-organic complexes such as Co-EDTA, which enhances the risk of radionuclide migration into groundwater if not properly treated [3].

To address these issues, the Chemical Oxidizing Reduction Decontamination (CORD) process based on MnO_4 is commonly used. This approach has been further developed into the High Permanganate-Chemical Oxidation Reduction Decontamination Ultraviolet (HP-CORD UV) process which has been widely adopted in light water reactors. This method is recognized for its high decontamination factor and its ability to break down organic acids through ultraviolet irradiation, making it suitable for both stainless and carbon steel [4]. The HP-CORD UV process typically comprises an initial oxidation step, where permanganate oxidized Cr(III) to Cr(VI), thereby improving the removal of metal oxides layers, followed by a cleaning phase utilizing oxalic acid and EDTA [4]. During these stages, released fission products (Sr-90 and Cs-137) are removed only by organic ion exchange resins (IERs) [5], while excess oxalic acid is subsequently decomposed using hydrogen peroxide under UV irradiation [4]. Despite its

effectiveness, the HP-CORD UV process generates large volumes of radioactive acidic liquid waste (RALW) containing radionuclides (Sr-90 and Cs-137), activated elements (Co-58, Co-60, Mn-54, Fe-55, Ni-63, and Cr-51), and corrosion products [5]. This necessitates further purification via organic IERs. The resultant radioactive spent IERs containing radionuclides are categorized as low- and intermediate-level radioactive waste and spent IERs must be immobilized using suitable binder matrix such as cement waste form [6]. However, the immobilization of spent IERs presents a significant challenge because their swelling property leads to the physicochemical degradation of cement waste form, thereby making them some of the most difficult radioactive wastes to manage and dispose of in the long term [6, 7]. Recent studies have investigated the immobilization of spent IERs using alkali- or acid-activated geopolymers [6-8]. These studies have focused on damp or water-saturated rather than dry spent IERs. Saturating spent IERs with water can reduce their expansion and mitigate degradation of the geopolymer matrix. Nonetheless, the actual waste loading of spent IERs remains lower than that of dry IERs [6-8]. This limitation is significant because the waste loading of the final waste form directly influences the economic feasibility of radioactive waste disposal. Other studies have explored pretreating spent IERs by thermal decomposition and milling them into ash or powder before immobilization in geopolymers [9, 10]. This method offers more stable immobilization of spent IERs but introduces challenges such as potential equipment contamination (e.g., mills, furnaces) and secondary radioactive waste generation during pretreatment process.

An alternative approach to managing radioactive acidic liquid waste (RALW) is direct immobilization with binder materials, thus eliminating the need for organic IERs. Conventional immobilization techniques utilize waste forms based on glass, polymer, or cementitious matrices. Of these, cementitious waste forms are widely favored internationally for the immobilization of radioactive wastes, owing to their combination of cost-effectiveness, ease of

handling, durability, and practical operational advantages [6, 12]. Despite their advantages, the structural integrity of cementitious waste forms fundamentally relies on the highly alkaline environment (pH > 12) generated by calcium compounds' hydration process [13]. As a result, incorporation of RALW into these matrices reduces the pH of cement pore solution, adversely affecting long-term durability through diminished structural integrity and incomplete hydration.

Alkali-activated materials (AAMs), often referred to as alkali-activated geopolymers and made from pozzolanic materials such as metakaolin and fly ash, can also be used as an alternative to cement [14, 15]. The AAMs are characterized by an amorphous aluminosilicate structure formed through the polycondensation reactions of aluminates and silicates, and the negative surface charge is compensated by alkaline cations (Na or K) [14]. They possess superior properties compared to cement, including enhanced compressive strength, thermal stability, chemical resistance, and acid resistance [16, 17]. Furthermore, they demonstrate excellent capabilities for immobilizing both radionuclides and radioactive waste [18, 19]. However, directly immobilizing RALW using AAMs is considered unsuitable. This is because RALW reduces the pH of alkaline activators (e.g., sodium/potassium silicate solutions). Since these activators are essential raw materials that drive polycondensation from raw material dissolution to AAM structure formation, their alkaline pH is essential [20]. RALW compromises this process by resulting in unfavorable low-pH conditions (< 9).

In terms of Cs immobilization, ceramic materials such as pollucite ($CsAlSi_2O_6$) can be promising candidates for immobilizing radioactive Cs due to their limited Cs leaching. However, producing monolithic pollucite waste forms requires pelletizing and a sintering process at 1400–1500 °C, where Cs volatilization can occur due to the high temperature [21]. Although pollucite can be synthesized at relatively low temperatures (below 100 °C) through hydrothermal synthesis based on interzeolite transformation of parent zeolites, it is difficult to fabricate it in a monolithic form [22]. Moreover, the charge-balancing Ca ions present in the

parent zeolite can form nanoscale aluminosilicate by-products, which may increase the Cs leaching [22]. Magnesium potassium phosphate cement (MKPC) waste forms immobilize Cs via Cs-struvite ($MgCsPO_4 \cdot 6H_2O$) formation but suffer drawbacks including rapid setting, excessive hydration heat, and binder expansion from persistent $MgKPO_4 \cdot 6H_2O$ formation at later ages [23, 24].

Recently, phosphoric acid-activated materials have garnered significant attention in the field of radioactive waste disposal. These materials, also known as phosphate-based geopolymers or amorphous aluminophosphate (AAP), are fabricated by the acid activation of metakaolin with phosphoric acid solution. The key distinction between AAPs and AAMs lies in their fundamental structural units. AAPs utilize aluminate and phosphate as primary building blocks which leads to the formation of amorphous aluminophosphate [25]. They exhibit higher early age compressive strength and greater thermal stability compared to AAMs [26]. Furthermore, monovalent cations for charge compensation are not required due to charge neutralization by the positive phosphorous unit [27]. Consequently, AAPs can be effectively utilized for managing various hazardous waste, including radioactive waste. Recent studies have demonstrated the immobilization of radioactive borate waste [28, 29], spent ion exchange resins [6], organic liquids [30], and radionuclides such as selenium and iodine [31] using AAPs. The acidic activator employed in the fabrication of AAPs consistently maintains an acidic pH, with the precise value dependent on the stoichiometric formulation. This property allows AAPs to immobilize RALW directly while maintaining an acidic pH in the resulting system, in contrast to cement and AAM waste forms which require an alkaline environment. Although the direct behavior of AAP waste forms under alkaline environments in deep geological repositories has not yet been fully characterized, their intrinsic mechanical and chemical advantages highlight their strong potential as promising waste form materials.

In this study, RALW generated from the HP-CORD UV process was directly immobilized

by using it as the mixing solution in AAP waste forms. Additionally, the influence of Cs, a fission product that can be present in RALW and is exclusively removed by IERs, on the nano-, micro-, and macrostructures of AAP waste forms and its immobilization mechanism were investigated.

2. Materials and methods

2.1 Synthesis of simulant radioactive acidic liquid waste

In this study, an ideal RALW simulant with fully decomposed organics was used to assess direct immobilization feasibility and understand the immobilization mechanisms of Cs. For synthesis of the simulant RALW which is generated from HP-CORD UV process, high grade commercial chemicals such as $FeCl_3$ (Sigma-Aldrich, 97%), $CrCl_3 \cdot 6H_2O$ (Acros Organics, 98%), $MnCl_2 \cdot 4H_2O$ (Junsei Chemical, 98%), and $Ni(NO_3)_2 \cdot 6H_2O$ (Junsei Chemical, 97%) were dissolved in deionized water (DIW) to achieve concentrations of 6500 ppm of Fe, 5000 ppm of Cr, 5000 ppm of Mn, and 5000 ppm of Ni. The mixture was stirred at 25 ± 1°C for 24 h to reach an equilibrium state.

2.2 Fabrication of AAP waste forms

The commercial metakaolin, DIW, and 85% H_3PO_4 solution were used as starting materials. According to the designed phosphorous to aluminum (P/Al) molar ratio and free water content (Table 1 and 2), DIW and phosphoric acid solution were stirred for 2 h before being mixed. The prepared acidic solution and metakaolin were then combined using a centrifugal mixer, with mixing and de-gassing durations of 4 minutes (1800 rpm) and 30 seconds (2100 rpm), respectively. The fresh AAP mixture was poured into plastic molds (Φ30–H60 mm) on a vibrator to eliminate trapped air bubbles, and the molds were sealed with plastic covers to prevent moisture loss. The AAP waste forms were cured at 25 °C for 5 days and then

at 60 °C for 1 day, allowing initial stabilization and initial setting at a lower temperature to prevent a sudden internal temperature increase that could lead to severe thermal cracking during the heat curing [29]. The fabricated AAP waste forms were denoted according to their formulations; for example, AAP1.1 indicates a waste form with a P/Al molar ratio of 1.1 (Table 1 and 2). Meanwhile, the mixing solution in the AAP waste form was replaced by simulant RALW to assess whether AAP waste forms can directly immobilize RALW, and these samples were referred to as amorphous aluminophosphate with RALW (AAL) (Table 1 and 2). In addition, 10.0 wt% Cs was introduced as CsCl into the waste forms with the highest mixing content (AAP1.4 and AAL1.4) to investigate the immobilization mechanism of Cs in the acid-activated waste form system. This higher Cs content was necessary to obtain sufficient signal intensity for characterization techniques, enabling a detailed investigation of Cs bonding environments within the AAP waste forms.

2.3 Sample characterization

Following a 7-day curing period, the compressive strength was determined. Three samples from each mix formulation were tested using an ST-1001 compression testing machine, with a constant loading rate of 0.6 MPa/s.

X-ray diffraction (XRD) patterns were collected on a Rigaku MiniFlex diffractometer (40 kV, 15 mA, Cu Kα radiation) to investigate mineralogical properties. The scans ranged from 5° to 65° 2θ with a 0.02° step size and 1°/min speed. Crystalline phases were identified using PDXL software with PDF-2 (2021) database.

Chemical bonding environments were analyzed by FT-IR spectroscopy (Nicolet iS10, ATR accessory) across 650–4000 cm^{-1}.

^{31}P MAS NMR spectra were measured with Bruker Avance III HD 400 MHz spectrometer (9.4 T). The 4 mm rotor was used and spinning frequency of 14 kHz was applied. The pulse

length and relaxation delay were 2 μs and 2 s, respectively. The spectra were obtained by accumulating 64 scans. ^{27}Al MAS NMR spectra were acquired at the UK high-field solid-state NMR Facility on a Bruker NEO 850 MHz spectrometer (20.0 T). The 4 mm rotor was used with spinning frequency of 12.5 kHz. The pulse length and relaxation delay were 1 μs and 1 s, respectively. The spectra were obtained by accumulating 256 scans. Two-dimensional ^{27}Al three quantum MAS (3QMAS) spectra were acquired using Z-filter sequence. The excitation pulse and the double frequency sweep conversion pulse were 10 and 20 μs, respectively. ^{133}Cs MAS NMR spectra were also acquired at the UK high-field solid-state NMR Facility on a Bruker NEO 850 MHz spectrometer (20.0 T). The 4 mm rotor was used with spinning frequency of 12.5 kHz. The pulse length was1 μs and relaxation delay was 20 s for the quantification of Cs binding sites. The spectra were obtained by accumulating 64 scans. ^{27}Al, ^{31}P, and ^{133}Cs spectra were referenced to 1.0 M aqueous CsCl, $AlCl_3$, and H_3PO_4 solutions, respectively, at 0 ppm. The deconvolution of ^{133}Cs MAS NMR spectra was performed using the DMFit software with the Czsimple model 32] to quantify the distribution of Cs binding environments based on isotropic chemical shift and quadrupolar coupling parameters.

Macro-scale elemental mapping of Al, Si, and Cs in samples was performed using laser-induced breakdown spectroscopy (LIBS, J200 Tandem). Point measurements were collected across a 15×15 grid (225 points) covering a 1.7 × 1.5 cm area on epoxy-embedded and polished sample surfaces. Each measurement used 15 shots at 30 mJ laser pulse energy.

A high-resolution field-emission scanning electron microscope (FE-SEM, JEOL JSM-7800F) and an energy-dispersive X-ray spectroscopy (EDS, Oxford Instruments Ultim detector) were utilized to obtain secondary electron images and elemental maps from the Pt-coated fracture surfaces.

Nanostructural analysis was performed using a Cs-corrected high-resolution scanning transmission electron microscope (HR-STEM, JEM-2200FS) equipped with EDS, operated at

an acceleration voltage of 200 kV. TEM samples were prepared by focused ion beam (FIB, FEI Nanolab G3 CX)/SEM using the H-bar lift-out method from gold-coated cross-sections, following tungsten sputtering of the region of interest (Figure. S1).

X-ray absorption near-edge structure (XANES) analysis was conducted at the 6D beamline of PLS-II (Pohang Accelerator Laboratory, South Korea). Cs L_{III}-edge spectra were acquired in fluorescence mode and calibrated against commercial CsCl and Cs_2CO_3 powder. Data processing and interpretation were utilized using ATHENA software [33].

3. Results and discussion

3.1 Mechanical strength and structural characteristics of AAP waste forms

The compressive strength of the AAP waste form after 7 days of curing met the criterion of compressive strength for waste forms in South Korea (≥3.445 MPa), while increased mixing solution content reduced compressive strength (Figure 1). In AAP waste forms, mixing solution serves as a blending medium, but excessive water dilutes the acid activator concentration as well. This leads to prolonged setting time and increased porosity, ultimately decreasing compressive strength (Figure 1) [34, 35]. The AAP waste form with the lowest mixing solution content exhibited the greatest variation in compressive strength. This outcome is attributed to the high viscosity and poor workability of the paste at low mixing solution content (21 wt%) which hindered effective mold filling process. Comparable behavior is commonly reported for AAMs [36].

Substituting mixing solution with RALW containing heavy metals did not significantly alter the compressive strength of AAP waste forms with all formulations exceeding the 3.445 MPa (Figure 1). This indicates that heavy metal ions in the RALW have negligible impact on the acid activation chemistry of AAP systems, demonstrating their efficacy in directly immobilizing RALW containing diverse heavy metals. The heavy metal immobilization

mechanisms in clay mineral-based AAM waste forms are known to include: (1) electrostatic attraction, (2) ion exchange, and (3) surface complexation [37]. Electrostatic attraction operates through interactions between surface charged adsorption sites and target elements [38]. In the AAP waste form system fabricated in this study, surface-mediated electrostatic attraction is unlikely to be a primary immobilization mechanism for heavy metal cations. This is because the surface of AAP waste form carries positive charge under pH 5 [31], while all heavy metal ions and fission products in the RALW exist as cationic species (e.g., Fe, Mn, Cr, Ni, and Cs), resulting in the incompatibility of the surface charge. In the AAP waste forms, a substantial quantity of exchangeable cations such as H^+ ions, are present to neutralize the negative charge at charge-balancing sites within the internal framework of tetrahedral Al unit (AlO_4^-) [39]. It has been previously reported that these cations facilitate ion exchange with heavy metal cations such as Pb, Cd, and Ni leading to their immobilization within the AAP waste form structure [39]. Furthermore, the immobilization of heavy metals is facilitated by surface complexation reactions occurring between hydroxyl functional groups, specifically Si–OH, P–OH, and Al–OH, present on the surface of the AAP waste form and the heavy metal ions [39]. Considering these aspects, heavy metal ions present in RALW are likely immobilized in AAP waste forms primarily through ion exchange and surface complexation.

The addition of Cs did not exert a substantial influence on the compressive strength of the AAP waste form (Figure 1). The AAP1.4 sample prepared with DIW as the mixing solution exhibited a compressive strength of approximately 19 ± 0.1 MPa, while AAP1.4Cs sample containing 10.0 wt% of Cs yielded a highly comparable strength of 19 ± 0.8 MPa. Although research on Cs-containing AAP waste forms remains limited, Tan et al. (2024) reported a marginal reduction of approximately 2% in compressive strength upon the addition of Cs at a concentration of 1.4 wt% relative to metakaolin. [40]. Previous research has proposed that Cs immobilization may occur through electrostatic attraction to anions such as $[PO_4]^{3-}$, $[HPO_4]^{2-}$,

$[H_2PO_4]^-$, and $[SiO_4]^{4-}$ [40]. However, in AAP waste forms under acidic conditions, the positively charged framework combined with low silicate solubility suggests that Cs immobilization primarily occurs through ion exchange with cations or physical incorporation within the three-dimensional dense gel matrix. Consequently, AAP waste forms exhibit no significant change in mechanical strength even when containing substantial quantities of heavy metals and Cs. This demonstrates the viability of directly immobilizing and utilizing RALW from HP-CORD UV process by using a mixing solution in AAP waste form formulation.

All AAP waste forms exhibited amorphous halos in X-ray diffraction patterns regardless of P/Al ratios, with the halo center positioned at approximately 28° 2θ region (Figure S2a). The amorphous aluminosilicate material which is the primary component of metakaolin displays a halo center near 22° 2θ that shifts to 25-30° 2θ following activation by the acid activator [20, 28]. The crystalline anatase originates from titanium oxide present as an impurity in the metakaolin. XRD analysis revealed that a fully amorphous phase was observed for the AAP waste forms prepared with either RALW or DIW, as well as for those containing Cs. Consistent with these observations, no new crystalline phases associated with heavy metals or Cs were identified (Figure S2). Therefore, it is inferred that both cationic heavy metals and Cs are incorporated into the amorphous aluminophosphate structure of the AAP waste form.

The FTIR analysis results closely aligned with the XRD findings (Figure S2b). The main band of the AAP waste form appeared asymmetrically within 960–1270 cm^{-1} irrespective of the P/Al ratio, centered near 1060 cm^{-1}. This band signifies rearrangement of aluminate and phosphate in the raw materials due to acid activation. The presence of the main band and an additional small band at 907 cm^{-1}, indicative of P–O–P bonding, confirms an aluminophosphate structure (Figure S2) [41]. The presence of Cs and use of RALW as mixing solution did not alter the chemical bondings of AAP waste forms (Figure S2b). The chemical bonds between phosphorus and heavy metals (or Cs) were not observed in the spectra (Figure

S2b).

3.2 Effect of RALW and Cs on the structure of AAP waste forms

Previous findings indicate that the mechanical strength of AAP waste forms is not significantly affected by direct immobilization of RALW using as mixing solution without any further treatment. Additional characterization was conducted on AAP1.4Cs and AAL1.4Cs samples with the highest mixing solution content (highest RALW content) and high Cs concentrations to better understand the effect of RALW and Cs on the structure of AAP waste forms.

For both AAP waste forms, ^{31}P MAS NMR analysis showed an asymmetrical single resonance at about -15 ppm (Figure S3), suggesting the existence of four-coordinated P (P^{IV}) which is a key structural component in aluminophosphates [29]. The chemical shift (ppm) is the change in the resonance frequency of a nucleus in NMR relative to a reference, determined by the electronic environment surrounding the nucleus. It is interesting to note that no discernible shielding or deshielding effects were seen in the NMR signals of the AAP1.4Cs which was fabricated using RALW. This implies that presence of heavy metal ions does not significantly affect the coordination environment of P. The P^{IV} and six-coordinated Al (Al^{VI}) are bonded to form aluminophosphate structure such as $[6Al(O–P)_x(O–Si)_y(OH)_{6-xy}]$ in AAP waste forms [25].

The ^{27}Al MAS NMR analysis of the two AAP waste forms revealed a primary resonance at approximately -10 ppm. This signal is attributed to the Al^{VI} bonded to P^{IV}, forming the aluminophosphate structure (Figure S3) [28]. In the ^{27}Al MAS NMR spectrum of AAP1.4Cs, minor resonances were observed at -4 ppm and -16 ppm, alongside the primary resonance (Figure S3). Given that the chemical shift range of approximately 10 to -30 ppm in ^{27}Al NMR typically corresponds to Al^{VI}, these signals are indicative of Al^{VI} species [25]. Considering the

presence of P^{IV} confirmed by the ^{31}P MAS NMR results (Figure S3) and previous study on AAP waste forms without Cs showing a single resonance at approximately -12 ppm [28], the presence of these two additional resonances suggests that the coordination environment of Al is altered by Cs. The solid-state MAS NMR resonances inherently provide detailed information regarding the coordination environment of the target element [42]. Therefore, although the Al coordination in the AAP waste form consistently remains six-coordination despite significant Cs content, the resonance shifts are likely due to changes in the local environment of Al such as the formation of Al^{VI}-O-Cs linkages. Further discussion will be provided in the ^{133}Cs MAS NMR section below.

These two peaks were not found in AAL1.4Cs sample, where only a single broad resonance was observed (Figure S3). The RALW contains various heavy metal ions; however, the ionic radii of Fe (1.26 Å) and Mn (1.35 Å) are larger than that of Al (1.25 Å), making it unlikely for them to substitute for Al in the octahedral sites of AlO_6 groups and form complexes. Although Cr and Ni can substitute for Al in crystalline spinel structures or form Ni^{IV}–O–Al^{VI} bonds [43], the AAP waste form has fully amorphous structure and does not contain a spinel (Figure S1). Therefore, the broadening of NMR signal is likely due to the paramagnetic effects of heavy metal ions rather than the formation of new structures. The presence of paramagnetic species such as metal ions in a sample can change its NMR spectrum by causing resonance signals to shift and broaden [44]. The unpaired electrons in these species act as strong relaxation agents, greatly increasing both the longitudinal (T_1, spin–lattice) and transverse (T_2, spin–spin) relaxation rates of nearby nuclear spins [45]. As a result, NMR signals often become much broader and may even disappear entirely. In addition, paramagnetic species can cause notable shifts in chemical shift values, known as paramagnetic shifts [44]. The impact of paramagnetic species on NMR signals depends on T_1 relaxation time of their unpaired electrons (T_1e) [45]. For ions with long T_1e values ($> 10^{-8}$ seconds), such as Fe^{3+}, Cr^{3+}, Mn^{2+}, and Cu^{2+},

their effect on nuclear relaxation is particularly strong, leading to especially pronounced broadening of NMR signals for nearby nuclei. Both AAP waste forms have the same stoichiometric molar ratios, differing only in the presence or absence of heavy metals. As a result, the coordination environment of Al, including the types and number of neighboring atoms and any structural distortions, could be modified by the heavy metal ions present in the RALW which would account for the observation of only a single ^{27}Al resonance in the AAL1.4Cs waste form.

^{27}Al 3QMAS NMR analysis was also performed to investigate whether immobilization of RALW resulted in changes to the local Al structure within the AAP waste form. In the sheared 3QMAS NMR, the horizontal projection is broadened by variations in the chemical shift, reflecting differences in the electronic environment around Al nuclei. In contrast, the vertical projection broadens due to quadrupolar interactions, reflecting local structural disorder, only when biphasic Q-shearing with factors of 3 and -4/9 is applied to the δ_3Q and δ_1Q axes [46]. Both AAP waste forms exhibited a center at approximately δ_3Q (F1) = 15 ppm and δ_1Q (F2) = -10 ppm, displaying similar asymmetric contours (Figure 2). In ^{27}Al 3QMAS NMR, the position of the center of gravity and the contour shape reflect the average Al coordination environment and the distribution of local electric field gradients, so the coincidence of these features in both AAP waste forms indicates that there is no significant difference in the Al environments between the two samples. This interpretation is supported by the ^{27}Al MAS NMR results, which show a predominant Al^{VI} resonance (Figure 2), consistent with Al being mainly present in an amorphous Al^{VI} environment. The close similarity in the F1 projection, F2 projection, and contour shapes between the two AAP waste forms suggests that using RALW as mixing solution does not significantly alter the local coordination environment of Al within the AAP waste form.

Meanwhile, ^{133}Cs MAS NMR analysis revealed distinct differences between the

AAP1.4Cs and AAL1.4Cs waste forms (Figure S3). The two asymmetric peaks were observed for AAP1.4Cs at 39.7 ppm and 8.47 ppm (Figure 3). These main peaks showed clear asymmetry and were broadly overlapped across a chemical shift range of approximately -35 to 100 ppm. The asymmetric and broad shapes of these peaks are likely due to the quadrupole effect because ^{133}Cs is a nucleus with a spin of 7/2. Solid-state ^{133}Cs MAS NMR studies on AAP waste forms are very limited and the Cs resonance peaks can appear at different chemical shifts depending on the material and structure in which Cs is immobilized. Previous work immobilized Cs using AAM waste forms prepared by alkali activation of metakaolin [47]. With changing Cs and network modifier cation (Na) contents, crystalline materials such as zeolite types A, X, and Y were formed together with the AAM waste form. These zeolites served as sites for Cs immobilization [47]. The ^{133}Cs MAS NMR peak positions depended on the zeolite types: zeolite A (−3.5, −14.5, 28 ppm), zeolite X (19.4, 64.6 ppm), and zeolite F (51.6, 64.6, 105.8 ppm) [47]. In the absence of Na ions (Cs_2O:Al_2O_3 ratio of 1), a peak at approximately 44 ppm was observed, corresponding to Cs immobilized within amorphous AAM structures [47]. The qualification of these peaks was performed by comparing the observed ^{133}Cs MAS NMR resonances with those from Cs-adsorbed zeolites. In another study, Cs was adsorbed onto montmorillonite, a layered silicate clay mineral, and the immobilization sites and mechanisms of Cs were investigated using density functional theory and high-field ^{133}Cs MAS NMR (18.8 T) [48]. The number of asymmetric Cs peaks increased proportionally with the extent of Cs ion exchange [48]. When montmorillonite was fully exchanged with Cs, three distinct peaks were clearly observed. The authors assigned these peaks as follows: Peak A (100 to -10 ppm) corresponds to Cs adsorbed near the center of the hexagonal cavity containing Al; Peak B (-30 to -70 ppm) corresponds to Cs adsorbed near the center of an empty hexagonal cavity; and Peak C (-100 to -140 ppm) corresponds to Cs adsorbed on the surface of open nanopores [48]. Whereas montmorillonite exhibits multiple immobilization sites for Cs at high exchange levels,

kaolin adsorption yields ^{133}Cs NMR peaks at 21 ppm and 47 ppm. These correspond to inner-sphere complexes (tightly bound sites) and outer-sphere complexes (loosely bonded sites), respectively [49]. However, AAP waste form has a differential structure compared to AAM waste forms and metakaolin is produced by calcining kaolin clay at high temperature. Although incomplete calcination may leave residual kaolin, quantitative analysis using the partial or no known crystal structure (PONKCS) analysis confirmed that the metakaolin used in this study is entirely amorphous phase without kaolin [36]. Therefore, the Cs immobilization mechanisms in this study are expected to differ from those reported in previous studies.

The peak at 39.7 ppm exhibits a larger full width at half maximum (FWHM) and more distinct asymmetry than the peak at 8.47 ppm (Figure S3), suggesting structural differences in Cs binding environments. Considering the main chemical composition of the AAP waste form, the elements that can bind with Cs, Al, and P, suggesting the possible formation of a structure such as cesium aluminophosphate. In this case, Cs would be directly bonded to Al which is a quadrupolar nucleus with a nuclear spin of 5/2. Quadrupolar nuclei possess an electric quadrupole moment that interacts with the surrounding electric field gradient (EFG) [42]. This quadrupolar coupling induces rapid nuclear relaxation, resulting in broadened NMR signals. If quadrupolar nuclei such as Cs and Al are directly bonded, the EFG around each nucleus is influenced by the presence of the other quadrupolar species. This leads to increased asymmetry and enhanced quadrupolar interactions, resulting in further broadening of the NMR signals. Therefore, the peak at 39.7 ppm strongly suggests the presence of direct bonding between Cs and aluminophosphate. In contrast, the peak at 8.4 ppm displays higher symmetry and a smaller FWHM (Figure S3). This indicates that Cs is immobilized within the AAP structure without direct bonding to aluminophosphate, resulting in weaker quadrupolar interactions. The narrow and symmetrical peak shape confirms that Cs is physically incorporated within the AAP framework, where reduced EFG permits a symmetrical NMR signal. Based on this, we assign

the 39.7 ppm peak to Cs bonded to aluminophosphate (Cs-Al-P bonded sites), and the 8.4 ppm peak corresponds to physically immobilized Cs within the AAP framework. The ^{133}Cs MAS NMR resonance in AAL1.4Cs exhibited a significant upfield shift and manifested as an extremely broad single peak spanning 120 to -50 ppm (Figure S3), appearing to merge two distinct peaks. This broadening is attributed to paramagnetic effects induced by heavy metal ions (Fe, Cr, Ni, and Mn) present in RALW, consistent with the mechanism discussed for the ^{27}Al MAS NMR results.

The quantitative analysis of ^{133}Cs MAS NMR spectra via DMFit simulation revealed that in AAP1.4Cs, 63.77% of Cs was assigned to Cs-Al-P bonded sites (39.7 ppm), while 31.09% corresponded to framework-incorporated Cs (8.4 ppm) (Figure 3). This distribution demonstrates that Cs immobilization preferentially occurs through direct bonding with aluminophosphate in the AAP waste form where reactive Al and P species dominate the coordination environment. For AAL1.4Cs, accurate deconvolution of the ^{133}Cs MAS NMR spectrum was challenging due to quadrupolar broadening effects. Nevertheless, the results revealed that the most prominent peak (65.87%) corresponds to Cs-Al-P bonded sites, consistent with the trend seen in AAP1.4Cs (Figure 3). These findings clearly show that Cs immobilization is primarily driven by binding with aluminophosphate, regardless of the presence of heavy metals in RALW (Table 3). Deconvolution also revealed a minor asymmetric peak at 54 ppm (Figure 3), attributed to Cs_2CO_3 formation from immobilized Cs reacting with atmospheric CO_2. In conventional AAMs, charge-balancing network modifiers typically remain confined within the AAM pore network. However, soluble alkali cations can diffuse outward, causing surface enrichment that facilitates alkali-carbonate formation (e. g, Na_2CO_3 and K_2CO_3) through CO_2 reaction [36]. The AAP waste form possesses a neutral or positive surface charge where Cs is immobilized through direct chemical bonding and physical incorporation into the AAP framework, rather than serving as a charge balancer that neutralizes

the aluminosilicate framework as in conventional AAMs. Consequently, a partial fraction of Cs physically incorporated in the AAP matrix migrates outward via diffusion, forming Cs_2CO_3 upon atmospheric CO_2 exposure (Table 3).

The XANES results provide atomic-level insights into Cs immobilization mechanisms in both AAP and AAL waste forms (Figure 3). It reveals oxidation states and coordination geometries by analyzing X-ray absorption edge shapes and positions of the target element. Although CsCl was used as the Cs source in this study, the XANES spectra for AAP and AAL waste forms closely resembled Cs_2CO_3 rather than CsCl (Figure 3). The oxidation state, coordination environment, and ligand type influenced on the XANES spectra [50]. The previous study on calcium aluminate cement containing CsCl has demonstrated that varying mix proportions alter Cs coordination environments, thereby modifying XANES spectra [50]. The XANES spectra of $CsNO_3$, Cs_2SO_4 and Cs_2CO_3 appear nearly identical despite the differing central atoms (N, S, and C) because in all cases Cs is coordinated by oxygen ligands, resulting in similar local environments around Cs [51]. This phenomenon arises as the resonance effect in polyatomic anions such as NO_3^-, SO_4^{2-} and CO_3^{2-} leads to negative charge being mainly localized on O atoms, suggesting the formation of an outer-sphere complex rather than a direct chemical bond between the ions. In accordance with the hard/soft acid/base theory, the hard acid Cs preferentially interacts with the hard base O^{2-} while showing lower affinity for the relatively softer central atoms [52]. The AAP and AAL waste form prepared at ambient and low temperatures under oxygen rich conditions features a high concentration of oxygen ligands around Cs and therefore forms Cs–O coordination. The XANES spectra from the AAP and AAL waste forms closely resembles that of Cs_2CO_3 even though the central bonding atoms differ because the oxygen ligand environment around Cs determines the observed spectrum. Furthermore, trace amounts of Cs_2CO_3 generated by reaction with atmospheric CO_2 as revealed in the ^{133}Cs MAS NMR analysis may also influence this resemblance; however, since the

amount of Cs_2CO_3 is only 0.3–0.5% of the total AAP waste form (Figure 3 and Table 3), the observed XANES spectra primarily reflect the bulk Cs–O coordination environment.

3.3 Macro-, micro-, and nano-scale characterizations of AAP waste form containing RALW and Cs

Macro-scale structural analysis of the AAP waste form was carried out using LIBS elemental mapping for Cs, Si, and Al, P which is one of the main elements of the AAP waste form could not be analyzed due to technical limitations of LIBS such as spectral interference from other elements and low detection limits. As a result, no significant structural differences in primary elements were observed between the two AAP waste forms (AAP1.4Cs and AAL1.4Cs) prepared with different mixing solution. Regions exhibiting high intensities for Cs and Al but low Si concentrations were identified in both AAP waste forms (Figure 4). This confirms that cesium aluminophosphate forms at the macro-scale and immobilizes Cs through bonding with aluminophosphate as indicated by the ^{133}Cs NMR results (Figure 3 and S3). Furthermore, the observation that Cs intensity levels are consistently intermediate or higher similar to Al and Si indicates homogeneous distribution and physical incorporation of Cs within the AAP waste form matrix (Figure 4). The regions with high Si intensity were identified resulting from dealumination during the initial reaction stage of the AAP waste form where Al is released from metakaolin leaving behind a residual Si layer. (Figure 4).

The morphology and chemical characteristics of the microstructure were examined by SEM analysis (Figure S4). Both AAP waste forms contained aggregates of various sizes ranging from tens of micrometers, and SEM images showed that these aggregates surrounded the AAP matrix (Figure S4). At low magnification (×1000), plate-like structures radiated from central points, resulting in flower-shaped structures. These plate-like structures were several micrometers in size and exhibited a layered structure with overlapping plates. At higher

magnification (×5000), the plate-like structures appeared very thin (estimated to be several hundred nanometers thick) with relatively wide lateral dimensions. The EDS elemental mapping showed that the radially arranged flower-like morphology was mainly composed of Al, P, Cs, and O while simultaneously revealing the homogeneous distribution of Cs in the AAP waste forms (Figure S4). This finding aligns with the ^{133}Cs MAS NMR and LIBS results (Figure 3 and 4) which showed Cs immobilization through bonding with aluminophosphate within the AAP waste form. The Si-rich phase arises from the dealuminated Si layer as previously discussed in the LIBS results. Considering the XRD results which confirm that AAP waste forms are an amorphous phase (Figure S2), the radially grown flower-like morphology exhibits directional growth but is considered amorphous phase or to have only short-range atomic ordering.

Microstructural analysis using backscattered electron (BSE) imaging revealed distinct contrast variations in both AAP waste forms supporting the ^{133}Cs MAS NMR results (Figure 5). Since BSE brightness correlates with atomic number, the brightest regions correspond to Cs as the heaviest element present. EDS mapping analysis of these bright areas confirmed high concentrations of Cs, Al, P, and O with minimal Si content (Figure 5). The bright zones correspond to cesium aluminophosphate formation where Cs bonds with Al and P as supported by ^{133}Cs MAS NMR results. Conversely, darker regions exhibit low Cs, Al, and P concentrations but dominant Si content. It is attributed to the Si layer and physically incorporated Cs (Figure 5). The EDS mapping demonstrates both homogeneous Cs dispersion throughout the AAP waste form matrix and the presence of cesium aluminophosphate phases.

Meanwhile, nano-scale analysis of Cs immobilization and nanostructural properties was conducted exclusively on AAP1.4Cs having a pure aluminophosphate structure since mixing solution type showed negligible impact on AAP waste form microstructures and macrostructures. The AAP1.4Cs prepared by FIB milling was analyzed via scanning

transmission electron microscopy in bright-field (STEM-BF) and high-angle annular dark-field (STEM-HAADF) modes allowing characterization from the surface to depths of tens of micrometers. BF imaging uses mass-thickness contrast so thicker regions or those containing heavy elements scatter more electrons and appear darker, while thinner or lighter regions appear brighter. HAADF imaging detects atomic number contrast so heavy atoms scatter electrons strongly and appear bright whereas light atoms appear dark. Therefore, the bright regions in BF images and dark regions in HAADF images of the AAP waste form indicate structures composed of relatively light elements such as Al, Si, and P (Figure S5). The observed layered structures in both images originate from the Si layer and unreacted metakaolin (Figure S5). Both BF and HAADF images also indicated a predominance of elements with higher atomic numbers, attributable to Cs as the largest element within the AAP1.4Cs waste form. These observations were further supported by EDS elemental mapping and demonstrated consistency with SEM/EDS results. STEM/EDS mapping indicated uniform distribution of Al and P throughout the AAP waste form, as well as localized Si-rich phases (e.g., Si layers) and unreacted metakaolin (Si and Al-rich regions) (Figure 6). Cs was homogeneously distributed with Al and P in the matrix but exhibited notable accumulation at the outermost surface (Figure 6).

To further investigate Cs immobilization within the nanostructure, high-resolution TEM (HRTEM) analysis was conducted across three regions based on STEM/EDS results (Figure 7). Region 1 corresponds to the Si-rich phase, which includes the Si layer and unreacted metakaolin; Region 2 represents the AAP waste form matrix where Cs is distributed; and Region 3 is the surface region with the highest Cs concentration (Figure 7). No lattice fringes indicative of crystalline structures were observed in the HRTEM images of all three regions. Fast Fourier transform and selected area electron diffraction analyses revealed a bright central spot surrounded by diffuse rings, confirming the amorphous nature of these regions. This result

545 is consistent with XRD analysis demonstrating a fully amorphous phase at the bulk level.
546 Therefore, at nano-, micro-, and macro-scale levels, Cs is not immobilized by forming specific
547 crystalline structures within the AAP waste form but rather by physical incorporation within
548 the waste form matrix or by forming amorphous cesium aluminophosphate.
549
550 **3.4. Further insights into Cs immobilization mechanism**
551 To investigate the early stages structural changes in AAP1.4Cs and AAL1.4Cs waste
552 forms, XRD and FTIR analyses were conducted at 30 minutes, 2 hours, 12 hours, and 24 hours
553 after mixing. Regardless of the mixing solution type, the XRD patterns of both AAP waste
554 forms exhibited no time-dependent changes and displayed a distinct amorphous hump and
555 crystalline anatase which is an impurity (Figure S6). This confirms that even at high Cs
556 concentrations, Cs does not precipitate as a crystalline phase in AAP1.4Cs and AAL1.4Cs
557 waste forms during early stages of reaction. This can be attributed to the challenging conditions
558 for crystalline phase formation in AAP1.4Cs and AAL1.4Cs waste forms, such as low pH and
559 limited silicate solubility. In contrast, AAMs can form crystalline Cs-aluminosilicate phases
560 like pollucite depending on curing conditions and target chemical composition [53]. In contrast
561 to XRD analyses showing identical diffraction patterns during initial reaction stages, FTIR
562 analysis revealed shifts in chemical bond positions over reaction time. No chemical bonding
563 associated with Cs or heavy metals from RALW was observed, regardless of reaction duration
564 or mixing solution type (Figure S7). However, the main band center was positioned near 980
565 cm^{-1} in early stage of reaction with a prominent asymmetric shoulder at 1060 cm^{-1}, differing
566 from the ~1060 cm^{-1} band center in cured AAP waste form (Figure S2, S6, and S7). These
567 features are attributed to aluminosilicate from unreacted metakaolin and aluminophosphate as
568 the primary structural component of AAP waste form, respectively. As curing progresses over
569 time, the band at 980 cm^{-1} gradually shifts to higher wavenumbers, ultimately positioning at

570 1060 cm^{-1} as an asymmetric band. The solid-state MAS NMR, TEM, and time-dependent
571 analyses collectively confirm that Cs is immobilized within the AAP waste form structure in
572 amorphous phase from the early stages of reaction throughout the curing process.

573 The *ex-situ* high-temperature XRD analysis provides further insight into Cs
574 immobilization mechanisms within AAP waste forms. Materials with short-range atomic
575 ordering and amorphous phases such as AAPs and AAMs present challenges for precise
576 understanding of structural evolution and reaction mechanisms. Therefore, heating amorphous
577 components to induce phase transitions followed by analysis of crystallized phases offers an
578 indirect approach to elucidating structural and crystallographic information [54]. For AAMs
579 having amorphous aluminosilicate structures, high-temperature treatment (>700 °C) induces
580 transformation into crystalline phases such as nepheline, Si-rich nepheline, kalsilite, and leucite,
581 depending on Si/Al ratios and alkali cation types [54]. XRD analysis of AAP waste forms
582 heated to 700°C showed reflections from crystalline phases as well as amorphous humps in
583 both samples (Figure S8). The amorphous hump indicates the amorphous structure of the AAP
584 waste form which would largely transform into crystalline phases at temperatures above 900°C
585 [54]. The crystalline phases consistently identified across both samples were aluminum
586 phosphate (PDF #01-072-7633, $AlPO_4$) and dicesium aluminum triphosphate (PDF #01-073-
587 9153, $Cs_2Al(P_3O_{10})$) (Figure 8). Therefore, the amorphous phase in the AAP waste form is
588 attributed to the amorphous aluminophosphate and Cs is immobilized by forming amorphous
589 $Cs_2Al(P_3O_{10})$ phase.

590 The waste forms developed for the disposal of radioactive waste must exhibit excellent
591 resistance to radionuclide leaching. According to the ANSI/ANS 16.1 leaching test which is
592 internationally used to evaluate the leaching characteristics of waste forms, the minimum
593 acceptable leachability index for Cs is 6.0 [28]. Recently, the long-term leaching test was
594 carried out on an AAP waste form containing 40 wt% spent IER that had adsorbed Cs (0.9 mg/g)

595 [28]. After 90 days, the cumulative fraction leached of Cs was approximately 15% ± 3.3,
596 yielding a leachability index of 8.9 ± 0.02 [28]. This value indicates significantly better Cs
597 retention compared with the ordinary Portland cement-based waste form, which exhibited a
598 leachability index of 6.8 [12]. Another study evaluated leaching rate of Cs from AAP waste
599 forms containing 2 wt% $CsNO_3$ relative to metakaolin [40]. After a 42-day leaching test, the
600 Cs leaching rate was 3.7 x 10^{-5} cm/d, notably lower than the limit of 4.0 x 10^{-3} cm/d specified
601 by the Chinese National Standard (GB14569.1-2011) [40]. Although AAP waste form may
602 show slightly lower Cs retention than alkali-activated materials and geopolymers, where Cs is
603 immobilized by electrostatic attraction to permanent negative surface charges, it has the
604 advantage of directly treating acidic RALW without pretreatment. While no specific
605 leachability index criteria exist for heavy metals, significant release of them is unlikely because
606 AAP primarily retains these elements via surface complexation and ion-exchange mechanisms.
607 Nevertheless, leaching behavior may vary depending on the type of leachant (e.g., groundwater,
608 seawater) and the presence of competing ions. Furthermore, during the HP-CORD UV
609 decontamination process, organic chelating agents are used to decompose metal oxides, and
610 trace amounts of undecomposed chelators may remain in the resulting RALW. These residual
611 organics could potentially influence the leaching of both heavy metals and radionuclides.
612 However, the present study assumed an ideal case in which all chelating agents were
613 completely decomposed, focusing instead on elucidating the Cs immobilization mechanism in
614 the AAP matrix through multiscale characterization. Future research is needed on immobilizing
615 RALW containing residual chelators and various radionuclides with long-term leaching
616 assessments to more accurately evaluate the potential use of AAP waste forms for radioactive
617 waste disposal.

618 The AAP waste form developed in this study, synthesized at 60°C under acidic
619 conditions, enables the immobilization of RALW that are difficult to treat with conventional

alkaline waste forms such as cement and AAMs. Replacing the mixing solution in the AAP waste form formulation with RALW directly immobilize the liquid waste without altering mechanical strength, chemical structure, or microstructure. Moreover, even with high concentrations of long-lived radionuclides such as Cs, it was successfully immobilized via chemical and physical immobilization. These results demonstrate that using the AAP waste form for immobilizing radioactive liquid waste can reduce the volume of secondary radioactive spent IERs. Furthermore, utilizing RALW as a raw material may facilitate the development of hybrid waste forms for co-immobilizing both liquid and solid radioactive wastes such as sludges, ion exchange materials, activated concrete, and metal waste, simultaneously. In terms of process scalability, AAP waste form is fabricated by a low-temperature process that is compatible with drum-scale cementation equipment but avoids the high-pH constraints of cement-based systems. Unlike vitrification, it does not require high-temperature melting or complex off-gas treatment, which reduces energy demand and capital cost. Consequently, the processing and infrastructure requirements for AAP waste forms are expected to be lower than those for glass waste forms and similar to those for cement waste forms. Although AAP waste form uses more expensive raw materials such as metakaolin, its ability to immobilize RALW at higher waste loadings than conventional cement waste form can make the overall treatment more cost-effective.

4. Conclusions

RALW produced by the HP-CORD UV process was used as a mixing solution and directly immobilized within the AAP waste form. The incorporation of RALW and Cs did not affect the mechanical strength of the AAP waste forms. There were no significant changes observed in crystallographic characteristics or chemical bonding. Solid-state MAS and MQMAS NMR analyses confirmed that neither RALW nor Cs substantially altered the local

environments of Al and P, the main structural components of the AAP waste form. Cs was immobilized via three primary mechanisms: (1) formation of cesium aluminophosphate, (2) physical incorporation into the AAP matrix, and (3) formation of Cs_2CO_3. DMFit simulations of ^{133}Cs MAS NMR spectra indicated that the formation of cesium aluminophosphate was the dominant immobilization pathway. Cs–O bonding within the waste form was attributed to contributions from both cesium aluminophosphate and carbonate phases. Multi-scale analyses showed that Cs was immobilized at the nano-, micro-, and macro-levels through the formation of amorphous cesium aluminophosphate and incorporation into the amorphous AAP matrix. Furthermore, Cs remained primarily immobilized within the amorphous phase throughout the early reaction. These findings demonstrate that unprocessed RALW can be effectively used as a mixing solution for AAP waste forms, potentially enabling the development of hybrid waste forms capable of co-immobilizing both liquid and solid radioactive wastes.

Acknowledgements

This work supported by Nuclear Global Fellowship Program through KONICOF funded by the Ministry of Science and ICT (Project No. 2022M2C7A1A03062813), UK Engineering and Physical Sciences Research Council (EPSRC), under grant EP/ Y029208/1, and Korea Spent Nuclear Fuel (iKSNF) and Korea Foundation of Nuclear Safety (KOFONS) grant funded by the Korea Government (Nuclear Safety and Security Commission, NSSC) (No. RS-2021-KN066120).

References

[1] J. Jung, H. Eun, S. Park, J. Park, N. Chang, S. Kim, B. Seo, S. Park, A study on the removal of impurities in a SP-HyBRID decontamination wastewater of the primary coolant system in a pressurized water reactor, J. Radioanal. Nucl. Chem. 2018, 318, 1339-1345. DOI:

10.1007/s10967-018-6219-0.

[2] S. Keny, A. Kumbhar, G. Venkateswaran, K. Kishore, Radiation effects on the dissolution kinetics of magnetite and hematite in EDTA-and NTA-based dilute chemical decontamination formulations, Radiat. Phys. Chem. 2005, 72 (4), 475-482. DOI: /10.1016/j.radphyschem.2003.12.055.

[3] S. Tandy, K. Bossart, R. Mueller, J. Ritschel, L. Hauser, R. Schulin, B. Nowack, Extraction of heavy metals from soils using biodegradable chelating agents, Environ. Sci. Technol. 2004, 38 (3), 937-944. DOI: 10.1021/es0348750.

[4] M. Corrado, S. Cao, S. Grassini, L. Iannucci, L. Savoldi, Optimization for the HP-CORD UV chemical decontamination process for AISI 304 stainless steel, Nucl. Eng. Des. 2023, 414, 112550. DOI: 10.1016/j.nucengdes.2023.112550.

[5] A. Rivonkar, R. Katona, M. Robin, T. Suzuki-Muresan, A. Abdelouas, M. Mokili, G. Bátor, T. Kovács, Optimisation of the chemical oxidation reduction process (CORD) on surrogate stainless steel in regards to its efficiency and secondary wastes, Front. Nucl. Eng. 2022, 1, 1080954. DOI: 10.3389/fnuen.2022.1080954.

[6] B. Kim, Y. Shin, S. Park, B. Walkley, S. Oh, J. Kang, W. Um, Assessment of structural stability and leaching characteristics of phosphate-based geopolymer waste form containing radioactive spent ion exchange resins, J. Nucl. Mater. 2025, 607, 155671. DOI: 10.1016/j.jnucmat.2025.155671.

[7] Y. Shin, B. Kim, J. Kang, H.M. Ma, W. Um, Estimation of radionuclides leaching characteristics in different sized geopolymer waste forms with simulated spent ionexchange resin, Nucl. Eng. Technol. 55 (2023) 3617–3627, DOI: 10.1016/j.net.2023.06.026.

[8] Lin, W., Chen, H., Huang, C., 2020. Performance study of ion exchange resins solidification using metakaolin-based geopolymer binder. Prog Nucl Energy 129, 103508. DOI: 10.1016/j.pnucene.2020.103508.

[9] Development of a new process for the radioactive ion exchange resins conditioning - HYPEX ®. Prog. Nucl. Energy, 180, 105639. DOI: 10.1016/j.pnucene.2025.105639.

[10] P. Perez-Cortes, I. Garcia-Lodeiro, M.C. Alonso, F. Puertas, Cementation of spent radioactive ion-exchange resin ashes using alkali-activated cements: physicochemical and structural changes, Cem. Concr. Compos. 149 (2024) 105517, DOI : 10.1016/j.cemconcomp.2024.105517.

[11] J. Li, J. Wang, Advances in cement solidification technology for waste radioactive ion exchange resins: a review, J. Hazard. Mater. 2006, 135 (1-3), 443-448. DOI: 10.1016/j.jhazmat.2005.11.053..

[12] J.G. Jang, S.M. Park, H.K. Lee, Physical barrier effect of geopolymeric waste form on diffusivity of cesium and strontium, J. Hazard. Mater. 2016, 318, 339-346. DOI: 10.1016/j.jhazmat.2016.07.003.

[13] K. Andersson, B. Allard, M. Bengtsson, B. Magnusson, Chemical composition of cement pore solutions, Cem. Con. Res. 1989, 19 (3), 327-332. DOI: 10.1016/0008-8846(89)90022-7.

[14] B. Walkley, X. Ke, O.H. Hussein, S.A. Bernal, J.L. Provis, Incorporation of strontium and calcium in geopolymer gels, J. Hazard. Mater. 2020, 382, 121015. DOI: 10.1016/j.jhazmat.2019.121015.

[15] S. Lee, H.-T. Jou, A. van Riessen, W.D.A. Rickard, C.-M. Chon, N.-H. Kang, Three-dimensional quantification of pore structure in coal ash-based geopolymer using conventional electron tomography, Constr. Build. Mater. 2014, 52, 221-226. DOI: 10.1016/j.conbuildmat.2013.10.072.

[16] B. Kim, J. Lee, J. Kang, W. Um, Development of geopolymer waste form for immobilization of radioactive borate waste, J. Hazard. Mater. 2021, 419, 126402. DOI: 10.1016/j.jhazmat.2021.126402.

[17] J.L. Provis, J.S.J. Van Deventer, Geopolymers: structures, processing, properties and

720 industrial applications, Woodhead Publishing, Cambridge, 2009.
721 [18] R.I. Chaerun, N. Soonthornwiphat, K. Toda, K. Kuroda, X. Niu, R. Kikuchi, T. Otake, Y.
722 Elakneswaran, J.L. Provis, T. Sato, Retention mechanism of cesium in chabazite embedded
723 into metakaolin-based alkali activated materials, J. Hazard. Mater. 2022, 440, 129732. DOI:
724 10.1016/j.jhazmat.2022.129732
725 [19] X. Niu, Y. Elakneswaran, R. Islam Chaerun, C. Fang, N. Hiroyoshi, J.L. Provis, T. Sato,
726 Development of metakaolin-based geopolymer for selenium oxyanions uptake through in-situ
727 ettringite formation, Sep. Purif. Technol. 2023, 324, 124530. DOI:
728 10.1016/j.seppur.2023.124530.
729 [20] B. Kim, S. Lee, Review on characteristics of metakaolin-based geopolymer and fast setting,
730 J. Korean Ceram. Soc. 2020, 57 (4), 368-377. DOI: 10.1007/s43207-020-00043-y.
731 [21] G. Y. Kim, B. Lee, J. H. Choi, J. K. Lee, H. W. Kang, J. Y. Pyo, J. H. Yang, H. S. Park, K.
732 R. Lee, Fabrication and evaluation of monolithic pollucite waste form for immobilization of
733 radioactive cesium, Ceramics International 51 (2025) 34248-34260. DOI:
734 10.1016/j.ceramint.2025.05.152
735 [22] S. Hong, W. Um, Risks of Nanoscale Byproducts Generated during the Interzeolite
736 Transformation for Cesium Sequestration, Chemistry of Materials 37 (2025) 1001-1012. DOI:
737 10.1021/acs.chemmater.4c02647.
738 [23] J. Y. Pyo, B. Lee, G. Y. Kim, H. W. Kang, J. H. Choi, H. S. Park, K. R. Lee, Cesium
739 immobilization in magnesium potassium phosphate cement: limited solid solution and
740 polymorphism of Cs-struvite, Ceramics International (2025). DOI:
741 10.1016/j.ceramint.2025.09.026.
742 [24] Y. Lv, T. Li, X. Xu, J. Yang, Y. Du, X. Hu, W. Chen, Effect of steel slag powder on the
743 sulfate corrosion behaviour of magnesium potassium phosphate cement slurry, Constr. Build.
744 Mater. 456 (2024) 139170. DOI: 10.1016/j.conbuildmat.2024.139170.

745 [25] H. Lin, H. Liu, Y. Li, X. Kong, Properties and reaction mechanism of phosphoric acid
746 activated metakaolin geopolymer at varied curing temperatures, Cem. Concr. Res. 2021, 144,
747 106425. DOI: 10.1016/j.cemconres.2021.106425.
748 [26] Y.-S. Wang, Y. Alrefaei, J.-G. Dai, Silico-Aluminophosphate and Alkali-Aluminosilicate
749 Geopolymers: A Comparative Review, Front. Mater. 2019, 6 (106), DOI:
750 10.3389/fmats.2019.00106.
751 [27] X. Niu, Y. Elakneswaran, N. Hiroyoshi, Surface chemistry and radionuclide anion
752 immobilisation potential of phosphoric acid-activated metakaolin-based geopolymers, Cem.
753 Conc. Res. 2024, 181, 107549. DOI: 10.1016/j.cemconres.2024.107549.
754 [28] B. Kim, J. Kang, Y. Shin, W. Um, Waste acceptance criteria testings of a phosphate-based
755 geopolymer waste form to immobilize radioactive borate waste, J. Nucl. Mater. 2023, 586,
756 154671. DOI: 10.1016/j.jnucmat.2023.154671.
757 [29] B. Kim, J. Kang, Y. Shin, T.-m. Yeo, W. Um, Immobilization mechanism of radioactive
758 borate waste in phosphate-based geopolymer waste forms, Cem. Conc. Res. 2022, 161, 106959.
759 DOI: 10.1016/j.cemconres.2022.106959.
760 [30] T. Dong, S. Xie, J. Wang, G. Zhao, Q. Song, Solidification and Stabilization of Spent
761 TBP/OK Organic Liquids in a Phosphate Acid-Based Geopolymer, Sci. Technol. Nucl. Install.
762 2020, 2020 (1), 1-7. DOI: 10.1155/2020/8094205.
763 [31] X. Niu, Y. Elakneswaran, A. Li, S. Seralathan, R. Kikuchi, Y. Hiraki, J. Sato, T. Osugi, B.
764 Walkley, Incorporation of boron into metakaolin-based geopolymers for radionuclide
765 immobilisation and neutron capture potential, Cem. Concr. Res. 2025, 190, 107814. DOI:
766 10.1016/j.cemconres.2025.107814.
767 [32] J.B. d'Espinose de Lacaillerie, C. Fretigny, D. Massiot, MAS NMR spectra of quadrupolar
768 nuclei in disordered solids: the Czjzek model, J. Magn. Reson. 2008, 192 (2), 244-251. DOI:
769 10.1016/j.jmr.2008.03.001.

770 [33] B. Ravel, M. Newville, ATHENA, ARTEMIS, HEPHAESTUS: data analysis for X-ray
771 absorption spectroscopy using IFEFFIT, J. Synchrotron Radiat. 2005, 12 (Pt 4), 537-541. DOI:
772 10.1107/S0909049505012719..
773 [34] V. Mathivet, J. Jouin, M. Parlier, S. Rossignol, Control of the alumino-silico-phosphate
774 geopolymers properties and structures by the phosphorus concentration, Mater. Chem. Phys.
775 2021, 258, 123867. DOI: 10.1016/j.matchemphys.2020.123867.
776 [35] Q. Tian, X. Yu, Y. Sui, L. Xu, Z. Lv, The Effect of Water on Metakaolin Phosphate-Based
777 Geopolymer Properties, Ceram. Silik, 66 (2022) 236-244. DOI: 10.13168/cs.2022.0018
778 [36] S. Lee, B. Kim, J. Seo, S. Cho, Beneficial Use of MIBC in Metakaolin-Based
779 Geopolymers to Improve Flowability and Compressive Strength, Materials (Basel) 2020, 13
780 (17), 3663. DOI: 10.3390/ma13173663.
781 [37] T. Zhang, W. Wang, Y. Zhao, H. Bai, T. Wen, S. Kang, G. Song, S. Song, S. Komarneni,
782 Removal of heavy metals and dyes by clay-based adsorbents: From natural clays to 1D and 2D
783 nano-composites, Chem. Eng. J. 2021, 420, 127574. DOI: /10.1016/j.cej.2020.127574.
784 [38] X. Niu, Y. Elakneswaran, C.R. Islam, J.L. Provis, T. Sato, Adsorption behaviour of
785 simulant radionuclide cations and anions in metakaolin-based geopolymer, J. Hazard. Mater.
786 2022, 429, 128373. DOI: 10.1016/j.jhazmat.2022.128373.
787 [39] Y. Liu, Y. Meng, X. Qiu, F. Zhou, H. Wang, S. Zhou, C. Yan, Novel porous phosphoric
788 acid-based geopolymer foams for adsorption of Pb (II), Cd (II) and Ni (II) mixtures: Behavior
789 and mechanism, Ceram. Int. 2023, 49 (4), 7030-7039. DOI: 10.1016/j.ceramint.2022.10.164.
790 [40] G. Tan, Z. Liu, X. Ma, Z. Zheng, G. Zhang, B. Wu, L. Zhang, L. Liu, Phosphoric acid-
791 activated metakaolin-based geopolymer: Optimizing P/A molar ratio to solidify Cs+ and Sr2+
792 in nuclear waste, Nucl. Eng. Des. 2024, 424, 113300. DOI: 10.1016/j.nucengdes.2024.113300.
793 [41] D. Bernasconi, A. Viani, L. Zárybnická, P. Mácová, S. Bordignon, C. Caviglia, E.
794 Destefanis, R. Gobetto, A. Pavese, Phosphate-based geopolymer: Influence of municipal solid

795 waste fly ash introduction on structure and compressive strength, Ceram. Int. 2023, 49 (13),
796 22149-22159. DOI: 10.1016/j.ceramint.2023.04.042.
797 [42] B. Walkley, J. Provis, Solid-state nuclear magnetic resonance spectroscopy of cements,
798 Mater. Today Adv. 2019, 1, 100007. DOI: doi.org/10.1016/j.mtadv.2019.100007.
799 [43] T. Tangcharoen, J. T-Thienprasert, C. Kongmark, Effect of calcination temperature on
800 structural and optical properties of MAl 2 O 4 (M= Ni, Cu, Zn) aluminate spinel nanoparticles,
801 J. Adv. Ceram. 2019, 8, 352-366. DOI: 10.1007/s40145-019-0317-5.
802 [44] R.J. Smernik, J.M. Oades, Effects of added paramagnetic ions on the CP/MAS NMR
803 spectrum of a de-ashed soil, Geoderma 1999, 89 (3-4), 219-248. DOI: 10.1016/s0016-
804 7061(98)00085-8.
805 [45] F.A. Bovey, P.A. Mirau, H. Gutowsky, Nuclear magnetic resonance spectroscopy, Elsevier,
806 1988.
807 [46] B. Walkley, G.J. Rees, R. San Nicolas, J.S.J. van Deventer, J.V. Hanna, J.L. Provis, New
808 Structural Model of Hydrous Sodium Aluminosilicate Gels and the Role of Charge-Balancing
809 Extra-Framework Al, J. Nucl Mater. 2022, 562, 153570. DOI: 10.1016/j.jnucmat.2022.153570.
810 [47] M. Arbel-Haddad, Y. Harnik, Y. Schlosser, A. Goldbourt, Cesium immobilization in
811 metakaolin-based geopolymers elucidated by 133Cs solid state NMR spectroscopy, J. Nucl
812 Mater. 2022, 562, 153570. DOI: 10.1016/j.jnucmat.2022.153570.
813 [48] T. Ohkubo, T. Okamoto, K. Kawamura, R. Guegan, K. Deguchi, S. Ohki, T. Shimizu, Y.
814 Tachi, Y. Iwadate, New Insights into the Cs Adsorption on Montmorillonite Clay from (133)Cs
815 Solid-State NMR and Density Functional Theory Calculations, J. Phys. Chem. A. 2018, 122
816 (48), 9326-9337. DOI: 10.1021/acs.jpca.8b07276.
817 [49] Y. Kim, R. James Kirkpatrick, 23 Na and 133 Cs NMR study of cation adsorption on
818 mineral surfaces: Local environments, dynamics, and effects of mixed cations, Geochim.
819 Cosmochim. Acta. 1997, 61 (24), 5199-5208. DOI: 10.1016/s0016-7037(97)00347-5.

[50] A. Iglesias-Juez, G.L. Chiarello, G.S. Patience, M.O. Guerrero-Pérez, Experimental methods in chemical engineering: X-ray absorption spectroscopy—XAS, XANES, EXAFS, Can. J. Chem. Eng. 2022, 100 (1), 3-22. DOI: /10.1002/cjce.24291.

[51] K. Koido, T. Iwasaki, K. Kurosawa, R. Takaku, H. Ohashi, M. Sato, Cesium-Catalyzed Hydrogen Production by the Gasification of Woody Biomass for Forest Decontamination, ACS Omega 2021, 6 (8), 5233-5243. DOI: 10.1021/acsomega.0c05237.

[52] A. Yamaguchi, M. Okumura, N. Kawamura, Y. Takahashi, Adsorption structures and bonding states of cesium and barium adsorbed on various sites of vermiculite, Sci. Total. Environ. 2025, 964, 178585. DOI: 10.1016/j.scitotenv.2025.178585.

[53] P. He, R. Wang, S. Fu, M. Wang, D. Cai, G. Ma, M. Wang, J. Yuan, Z. Yang, X. Duan, Y. Wang, D. Jia, Y. Zhou, Safe trapping of cesium into doping-enhanced pollucite structure by geopolymer precursor technique, J. Hazard. Mater. 2019, 367, 577-588. DOI: 10.1016/j.jhazmat.2019.01.013.

[54] B. Kim, B. Walkley, J.L. Provis, H.-m. Ma, W. Um, Effect of Ca (OH) 2 on the immobilization of simulated radioactive borate waste in metakaolin-based geopolymer waste forms, Cem. and Concr. Res. 2025, 197, 107946. DOI: 10.1016/j.cemconres.2025.107946.

837 **Table 1**. Mix formulations of AAP and AAL waste forms

Sample	Molar ratio	Mixing solution content (wt%)	Mixing solution type
AAP0.8	$2.0SiO_2$:$1.0Al_2O_3$:$0.8P_2O_5$:$7.7H_2O$	17.3	DIW
AAP1.1	$2.0SiO_2$:$1.0Al_2O_3$:$1.1P_2O_5$:$8.7H_2O$	19.6	
AAP1.4	$2.0SiO_2$:$1.0Al_2O_3$:$1.4P_2O_5$:$10.8H_2O$	21.2	
AAP1.4Cs*	$2.0SiO_2$:$1.0Al_2O_3$:$1.4P_2O_5$:$10.8H_2O$:$0.3Cs_2O$	21.2	
AAL0.8	$2.0SiO_2$:$1.0Al_2O_3$:$0.8P_2O_5$:$7.7H_2O$	17.3	RALW
AAL1.1	$2.0SiO_2$:$1.0Al_2O_3$:$1.1P_2O_5$:$8.7H_2O$	19. 6	
AAL1.4	$2.0SiO_2$:$1.0Al_2O_3$:$1.4P_2O_5$:$10.8H_2O$	21.2	
AAL1.4Cs*	$2.0SiO_2$:$1.0Al_2O_3$:$1.4P_2O_5$:$10.8H_2O$:$0.3Cs_2O$	21.2	

838 * Cs was added at 10.0 wt% of the total mixture weight

839

840 **Table 2**. Formulation details of AAP and AAL waste forms

Sample	Metakaolin (g)	Mixing solution (g)	85% H_3PO_4 solution (g)	CsCl (g)
AAP0.8	95.45	78.14	36.40	-
AAP1.1	80.77	88.16	41.07	-
AAP1.4	70.00	44.49	95.51	-
AAP1.4Cs*	70.00	44.49	95.51	26.63
AAL0.8	95.45	78.14	36.40	-
AAL1.1	80.77	88.16	41.07	-
AAL1.4	70.00	44.49	95.51	-
AAL1.4Cs*	70.00	44.49	95.51	26.63

841

842

843 **Table 3**. Cs immobilization fractions derived from DMFit simulation of ^{133}Cs MAS NMR

844 spectra

Sample	Cs-Al-P binding (%)	Physical incorporation (%)	Cs_2CO_3 (%)
AAP1.4Cs	63.77	31.09	5.14
AAL1.4Cs	65.87	30.42	3.72

845

846

847

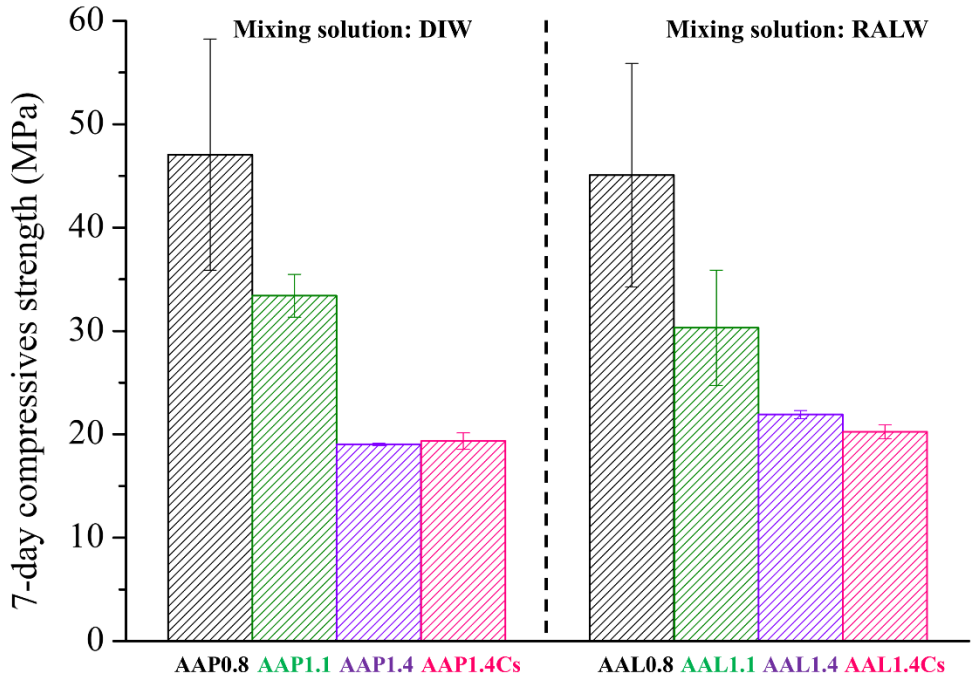

848

849 **Figure 1.** 7-day compressive strength of AAP waste forms with different mixing waters and at

850 varying P/Al ratios

851

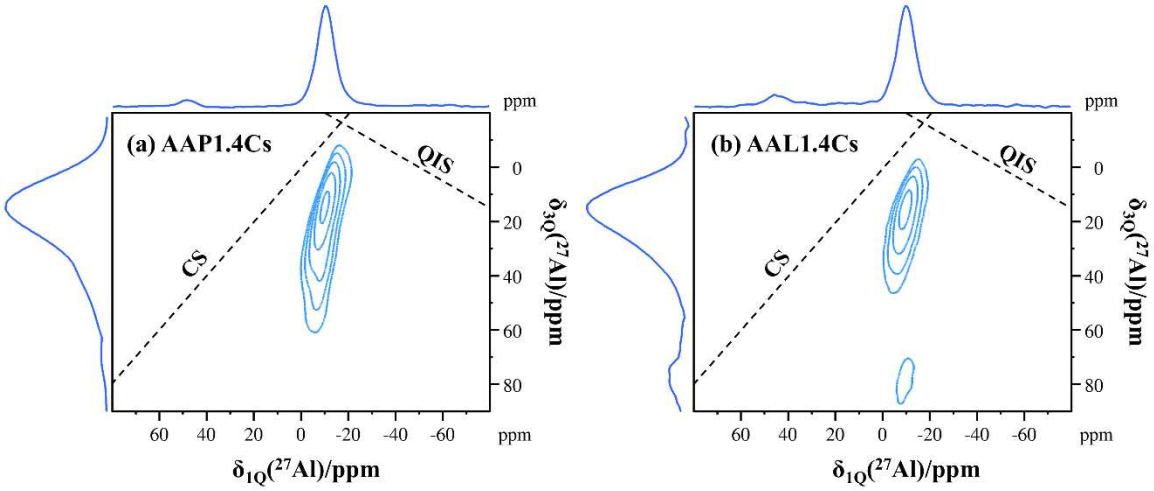

852

853 **Figure 2.** ^{27}Al 3QM MAS NMR results of AAP1.4 (a) and AAL1.4 (b); The chemical shift (CS)
854 and quadrupolar induced shift (QIS) axes are indicated by dotted and dashed lines,
855 respectively.

856

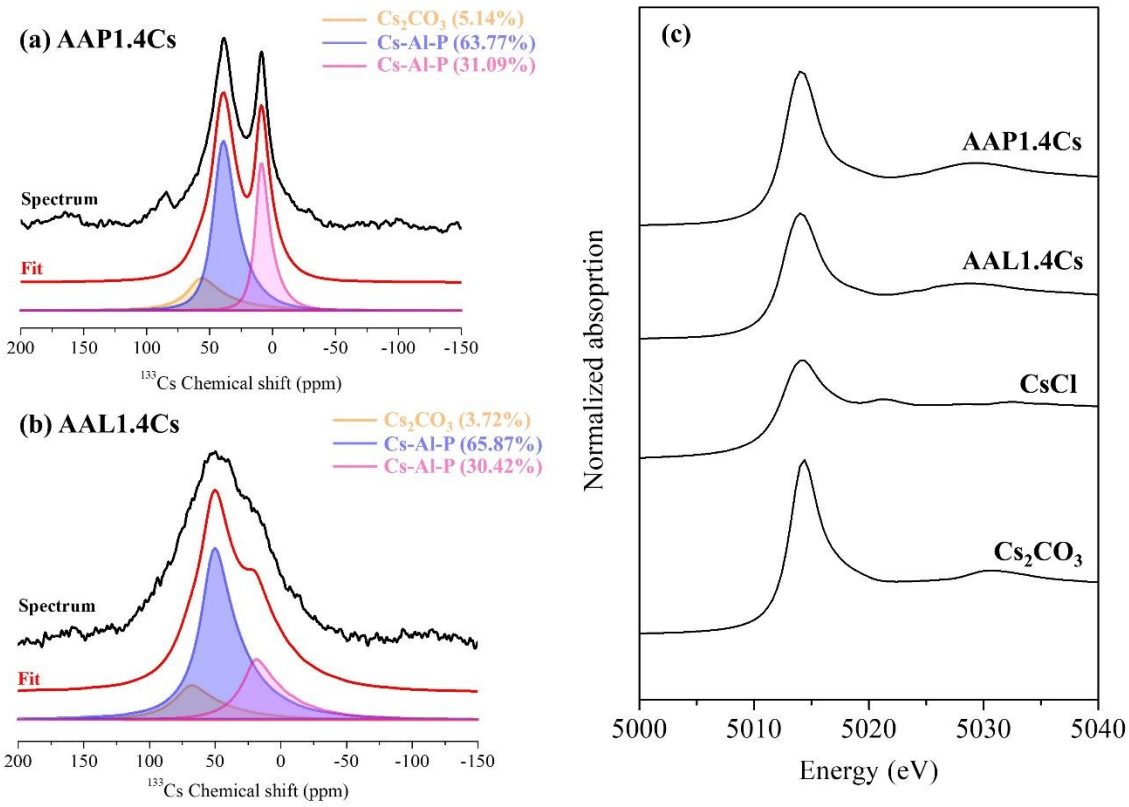

857

858 **Figure 3.** ^{133}Cs MAS NMR spectra for (a) AAP1.4Cs and (b) AAL1.4Cs, and normalised Cs
859 L_{III}-edge XANES spectra for AAP waste forms and reference materials.

860

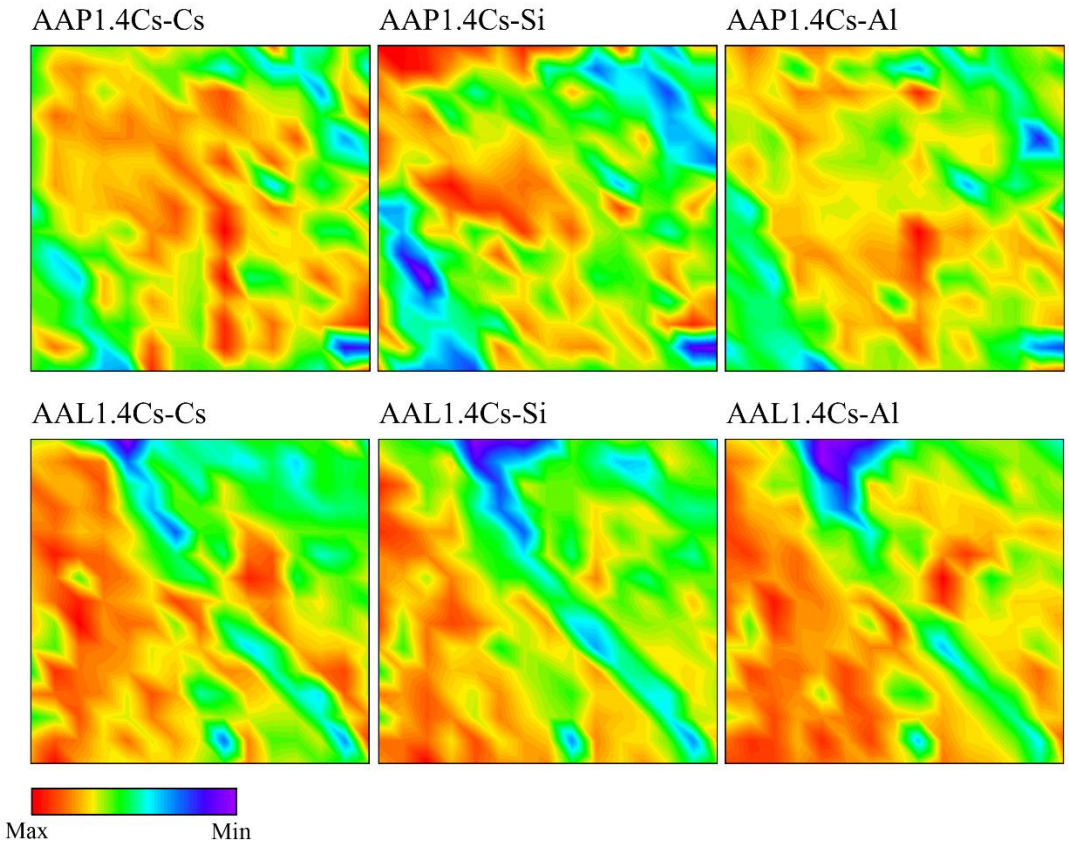

861

862 **Figure 4.** LIBS elemental mapping results of AAP1.4Cs and AAL1.4Cs

863

864

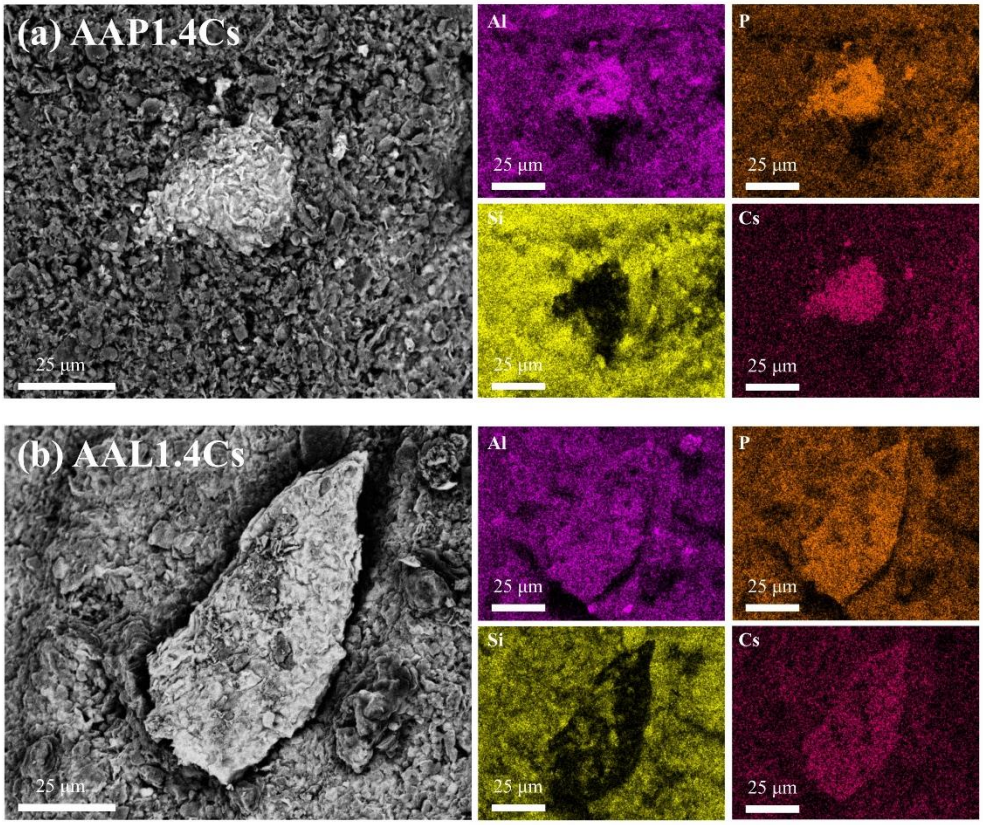

865

866 **Figure 5.** BSE images and EDS elemental mapping results of AAP1.4Cs and AAL1.4Cs

867

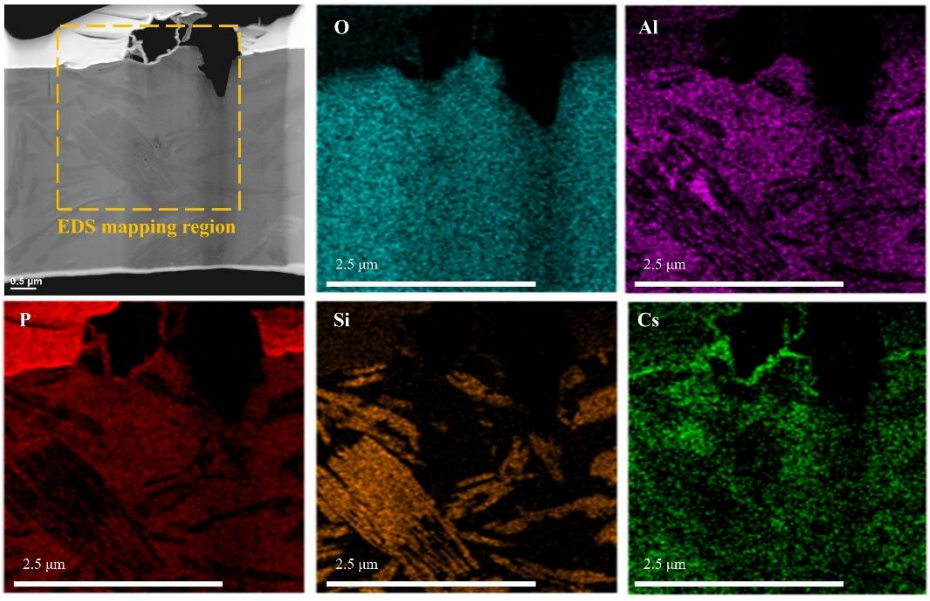

868

869 **Figure 6.** STEM-HAADF image and EDS elemental mapping results of AAP1.4Cs

870

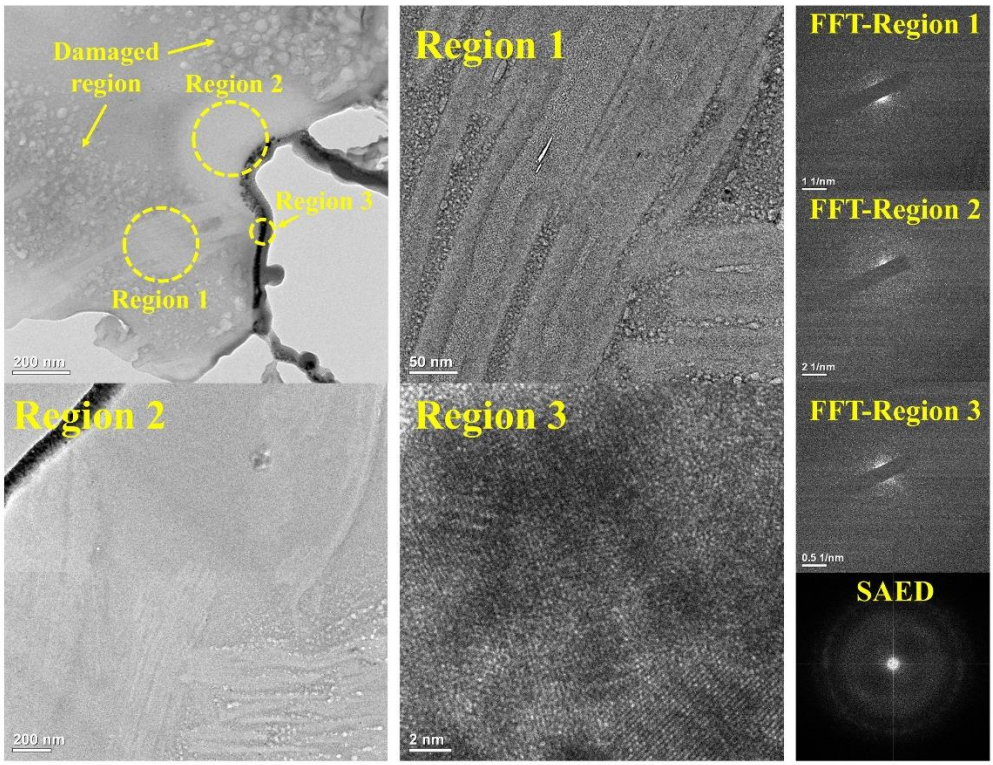

871

872 **Figure 7.** HR-TEM, FFT, and SAED images of AAP1.4Cs; Si-rich phase (region 1), AAP waste

873 form matrix (region 2), and surface region with high Cs concentration (region 3)

874

875

876

877